ROYAL SOCIETY
OF CHEMISTRY

Interlayer bond polarizability model for interlayer phonons in van der Waals heterostructures†

Rui Mei,[a,b] Miao-Ling Lin, [ID] [a] Heng Wu, [ID] [a,b] Lin-Shang Chen,[a] Yan-Meng Shi,[a] Zhongming Wei [ID] [a] and Ping-Heng Tan [ID] *[a,b]

Raman scattering provides essential insights into phonons, electronic structures and electron–phonon coupling within solids through the intensity of Raman peaks, which cannot be easily quantified using the classical bond polarizability model. The interlayer bond polarizability model (IBPM) had been developed to understand the Raman intensity of layer-breathing modes (LBMs) in two-dimensional materials. However, the quantitative understanding of the LBM intensity of a van der Waals heterostructure (vdWH) remains challenging. Here, in polynary vdWHs comprising twisted multilayer graphene (tMLG), MoS_2 and hBN, we observed a series of LBMs, whose intensity is markedly dependent on the excitation energy and twist angle of the tMLG constituent. An improved IBPM is proposed to quantitatively understand the Raman intensity of LBMs in the tMLG-based vdWHs, including the emergence or absence of a specific LBM when the excitation energy is resonant with the electronic states of tMLG or MoS_2 constituents. This work underscores the significant potential of the improved IBPM in accurately understanding and predicting the intensity profile of LBM in polynary vdWHs, even for the case of Raman scattering with excitation energies selectively resonant with the electronic states of the corresponding specific constituents.

1. Introduction

Raman scattering is one of the most important effects arising from the interaction between photons, electrons and quasi-particles (*e.g.*, phonons), which has been extensively studied and is an efficient and non-destructive analytical technique.[1,2] A rigorous quantitative analysis of relative intensities in Raman scattering provides foundational insights into electronic structures, and electron–phonon coupling (EPC) in solids.[3–5] According to the classical theory of Placzek approximation in solids,[3,6] Raman scattering of phonons results from the fluctuations in polarizability caused by lattice vibrations. Nowadays, with the development of advanced first-principles density functional theory (DFT) calculations, highly precise frequency and atomic displacement patterns for phonon modes in crystals can be obtained. However, in contrast to the purely vibrational calculation on phonon frequency, the quantitative calculation of Raman intensity is extremely complex.[7] The

empirical bond polarizability model had been introduced to predict the Raman intensities of various materials, *e.g.*, fullerenes, graphene ribbons and two-dimensional materials (2DMs).[5,7–12] In this model, the Stokes Raman intensity I is proportional to the square of the change of the system's polarizability ($\Delta\alpha$) as follows:[5,10–12] $I \propto \frac{n_q + 1}{\omega_q}|\Delta\alpha|^2$, where n_q and ω_q are the phonon occupation according to Bose–Einstein statistics and peak position of the corresponding phonon mode, respectively. $\Delta\alpha$ is the sum of the polarizability change of the corresponding system.

In general, the polarizability can be approximated by the sum of individual bond polarizability from all the bonds in a unit cell.[7,10,12] It becomes complex for a large size of a unit cell with many atoms. In this case, the quantitative determination of total polarizability change becomes computationally intensive and less accurate.[7] Encouragingly, within the domain of two-dimensional materials (2DMs) and binary van der Waals heterostructures (vdWHs), the bond polarizability model can be significantly simplified when discussing their unique interlayer phonons[13,14] which are important indicators of interface coupling and stacking order.[5,12] For the interlayer phonon in 2DMs or binary vdWHs, each layer vibrates rigidly and thus it can be simplified as a single rigid body, where the structural details within each layer can be generally omitted.[13,14] Since the bonds within each layer (intralayer bonds) are not compressed/stretched for the interlayer vibrations, they do not con-

[a] *State Key Laboratory of Superlattices and Microstructures, Institute of Semiconductors, Chinese Academy of Sciences, Beijing 100083, China. E-mail: phtan@semi.ac.cn*
[b] *Center of Materials Science and Optoelectronics Engineering & CAS Center of Excellence in Topological Quantum Computation, University of Chinese Academy of Sciences, Beijing 100049, China*
†Electronic supplementary information (ESI) available: Further details of the samples and linear chain model. See DOI: https://doi.org/10.1039/d3nr06437a

tribute to the change of the polarizability induced by interlayer phonons.[12] Such an empirical method for interlayer phonons is referred to as the interlayer bond polarizability model (IBPM). Note that interlayer phonons in 2DMs can be divided into the shear mode (S) and layer-breathing mode (LBM), according to the relative motion direction of adjacent rigid layers, either perpendicular or parallel to their normal.[13,14] In particular, the S modes and LBMs of vdWHs possess totally different characteristics. For instance, the S modes are usually localized within specific constituents because of the absence of an overall in-plane restoring force at the interface,[15] but the LBMs involve the contribution from all the layers in the vdWH.[5,16,17] Previous studies on IBPM have shown its availability to predict the Raman intensity of S modes and LBMs in 2DMs and binary vdWHs, *e.g.* transition metal chalcogenides (TMDs), graphene flakes, and hBN/WS$_2$ vdWHs.[5,10–12]

At present, the most advanced optoelectronic devices based on 2DMs are usually polynary systems. Besides the functional layers, the electrode, substrate and encapsulated layers can also be involved together to improve the device performance. The interfacial coupling between the adjacent constituents of these layers is crucial to the device performance. Since the LB vibration is extended to the whole vdWH, the LBM can be used as a fingerprint to probe the interfacial coupling by its peak position and Raman intensity.[18] Therefore, improving IBPM to quantitatively evaluate the LBM intensity is a critical issue for optoelectronic devices based on polynary vdWHs. Furthermore, graphene layers had been widely used as an electrode for vdWH-based optoelectronic devices, or as a wafer for van der Waals epitaxy toward high quality semiconductor films.[19] Twisted multilayer graphene (tMLG) is a special vdWH and offers a unique opportunity to manipulate its band structure by changing its stacking order and twist angle (θ_t).[15,20,21] For example, its van Hove singularities (VHSs) in the joint electronic density of states (JDOS) can be tuned across a broad energy spectrum by varying θ_t.[22,23] Such tunability of VHSs in tMLG holds substantial potential for tunable optoelectronic devices.[24] Therefore, compared with the IBPM under non-resonant conditions, it is also necessary to improve the IBPM to understand well the LBM intensity of tMLG-based polynary vdWHs once the excitation energy is resonant with the VHS transition energy of tMLG.

Here, tMLG-based polynary vdWHs, *e.g.*, tMLG/MoS$_2$ vdWHs, show a series of LBMs, exhibiting strong coupling with the electronic states confined within MoS$_2$ or tMLG constituents. The Raman intensity profiles of the LBMs is sensitive to the θ_t of tMLG. Similar results are also present in other ternary vdWHs (*e.g.* hBN/tMLG vdWHs) and quaternary vdWHs (*e.g.* hBN/tMLG/MoS$_2$ vdWHs). By considering the contribution from multiple interfaces and the resonance from VHSs of JDOS in standalone 2DM and tMLG flakes, we improve the IBPM of standalone 2DM flakes to tMLG-based polynary vdWHs to understand the intensity profile of the corresponding LBMs. The improved IBPM can well reproduce the intensity profiles of the LBMs observed in tMLG-based polynary vdWHs, *e.g.*, tMLG/MoS$_2$, hBN/tMLG and hBN/tMLG/

MoS$_2$. The emergence and absence of a specific LBM is also understood *via* the improved IBPM by considering the corresponding atomic displacements. This study exhibits the potential of the improved IBPM to theoretically predict the intensity profiles of LBMs in polynary vdWHs.

2. Experimental section

2.1. Sample preparation

Few-layer graphene, MoS$_2$, and hBN flakes were mechanically exfoliated from the corresponding bulk crystals onto 90 nm SiO$_2$/Si substrates. The layer number (N) of few-layer graphene ($N < 5$) flakes was identified by analyzing the line shape of the 2D peak,[25] whereas those of hBN and MoS$_2$ flakes were distinguished using peak positions of the interlayer phonons[5,14] in hBN-based vdWHs and standalone MoS$_2$ flakes, respectively. For the heterostructure fabrication, a nail polish-coated polydimethylsiloxane (PDMS) block mounted on a glass slide was utilized to pick up and release 2DMs.[26,27] The vdWHs were meticulously constructed layer by layer in specific order, by employing a nanomanipulator. m-layer (mLG, Bernal stacking if $m > 1$) and n-layer (nLG, Bernal stacking if $n > 1$) flakes were assembled with a twist angle (θ_t) to create a ($m+n$)-layer twisted system, denoted as t($m+n$)LG(θ_t). Here, θ_t can be determined by the R mode frequency of twisted multilayer graphene.[21] Moreover, m-layer hBN and n-layer MoS$_2$ were abbreviated as mL-hBN and nLM, respectively. Following this notation, t($m+n$)LG(θ_t)/kLM indicates a vdWH constructed with t($m+n$)LG(θ_t) and k-layer MoS$_2$. A large lattice mismatch between graphene and MoS$_2$ makes the moiré superlattices absent at the graphene/MoS$_2$ interface. Thus, the twisted angle between tMLG and MoS$_2$ is not intentionally fixed during the fabrication process. All the fabricated samples were subjected to annealing under vacuum conditions (approximately 10^{-7} hpa) at 300 °C for 2 hours to achieve an ideal interfacial coupling in vdWH. Optical images and AFM images of the samples are available in section I of the ESI.†

2.2. Raman measurements

Raman spectra were measured under a backscattering configuration at room temperature with a Jobin–Yvon HR800 Raman system, equipped with a liquid-nitrogen-cooled charge-coupled device (CCD) and a 100× objective (NA = 0.90). The excitation energies are 2.71 eV, 2.54 eV and 2.41 eV from Ar$^+$ laser, 2.33 eV from a diode-pumped-solid-state laser, 2.18 eV, 2.08 eV and 2.02 eV from a C-wave GTR laser (HÜBNER Photonics GmbH), and 1.96 eV from a He–Ne laser. 2400 lines per mm grating was used in Raman measurements to obtain high spectral resolution. The laser plasma lines were removed using a BragGrate bandpass filter from OptiGrate Corp., and the Rayleigh line was suppressed using three BragGrate notch filters (OptiGrate Corp.), which enable the measurement limit down to 5 cm^{-1} for each excitation energy.[13,14]

3. Results and discussion

3.1. Observation and assignment of LBMs in tMLG-based vdWHs

At first, we reveal the Raman characteristic features of typical vdWHs that were constructed with MoS_2, t(m+n)LG and hBN flakes, as shown in Fig. 1(a). Fig. 1(b) shows the Raman spectra of 2LM, t(3+1)LG(13°), t(3+1)LG(13°)/2LM, t(2+1)LG (13°), t(2+1)LG(13°)/2LM, 44L-hBN/t(2+1)LG(15°) and 44L-hBN/t(2+1)LG(15°)/2LM under excitation with energy (E_{ex}) of 2.33 eV. Intralayer phonon modes of each constituent appear in the high-frequency region (>150 cm^{-1}), including the A_{1g} and E_{2g}^1 modes of 2LM, and the G and R modes of t(m+n)LG. The corresponding Raman spectra of the vdWH nearly replicate the sum of those typical intralayer modes observed in each constituent since the interfacial coupling is significantly weaker than the intralayer bonding. Additionally, the interlayer modes including S and LBMs emerge in the low-frequency region (<150 cm^{-1}). For an in-plane isotropic 2DM with N rigid layers, there are $N − 1$ degenerate S modes and $N − 1$ LBMs, which are denoted as $S_{N,N−i}$ and $LBM_{N,N−i}$ ($i = 1, 2,..., N − 1$), respectively, where the $S_{N,1}$ ($LBM_{N,1}$) (*i.e.*, $i = N − 1$) is the one with the highest frequency and $S_{N,N−1}$ ($LBM_{N,N−1}$) (*i.e.*, $i = 1$) is the one with the lowest frequency. The S mode of 2LM ($S_{2,1}$) is observed at 22.5 cm^{-1}. The shear mode has previously been referred to as the C mode in graphene-based materials because it was first observed in AB-stacked multilayer graphene as a direct measurement of the interlayer *coupling*.[13] To distinguish the shear modes of tMLG from those of other 2DM constituents or flakes, here we denote the shear modes in tMLG as C modes. Therefore, the $C_{2,1}$ mode in t(2+1)LG and

the $C_{3,1}$ and $C_{3,2}$ modes in t(3+1)LG are observed at 31.8 cm^{-1}, 36.8 cm^{-1} and 21.8 cm^{-1}, respectively. The S or C modes of the corresponding constituents are also present in tMLG-based ternary and quaternary vdWHs, almost at the identical peak positions to those of 2LM and tMLG. The shear vibrations remain localized within specific constituents due to the negligible shear coupling at the interface of vdWHs.[15] However, the LBMs observed in ternary and quaternary vdWHs exhibit different peak positions from those of standalone 2LM and t(m+n)LG. In particular, according to previous reports,[5,18] standalone mL-hBN exhibits no observable LBMs due to the extremely weak EPC strength when subjected to visible laser excitation. However, based on the cross-dimensional EPC effect,[5] a series of LBMs are experimentally observed in the low frequency region in 44L-hBN/t(2+1)LG(15°) and 44L-hBN/t(2+1) LG(15°)/2LM, whose atomic displacements involve all the layers of the corresponding vdWH, including 44L-hBN, t(2+1) LG and 2LM constituents. The corresponding Raman spectra exhibit ripple-like intensity profiles.

The linear chain model (LCM) has been widely used to predict the frequencies of the S modes and LBMs in 2DMs and vdWHs, where only the nearest-neighbor interaction between adjacent rigid layers is considered.[5,13–17] However, the improved linear chain model (2LCM) considering the interaction between second nearest-neighbor graphene layers is necessary to predict the LBMs in multilayer graphene (MLG), t(m+n)LG and related vdWHs.[5,16–18] Based on the 2LCM, we calculated the LBM frequencies of t(3+1)LG, t(3+1)LG/2LM, t(2 +1)LG, t(2+1)LG/2LM, 44L-hBN/t(2+1)LG and 44L-hBN/t(2+1) LG/2LM vdWHs using the previously reported force constants,[18] and have shown the calculated data in Fig. S2 of the
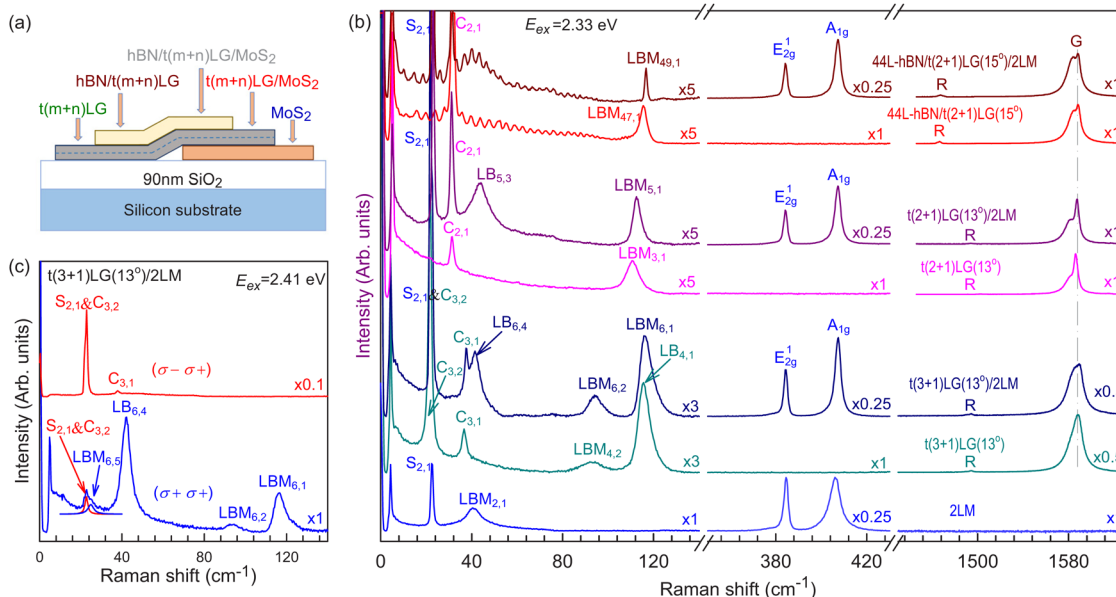
Fig. 1 (a) Structural schematic of typical vdWHs that are assembled by MoS_2, t(m+n)LG and hBN. (b) Raman spectra of 2LM, t(3+1)LG(13°), t(3+1)LG (13°)/2LM, t(2+1)LG(13°), t(2+1)LG(13°)/2LM, 44L-hBN/t(2+1)LG(15°) and 44L-hBN/t(2+1)LG(15°)/2LM under excitation of a 2.33 eV laser. (c) S(C) modes and LBMs of t(3+1)LG(13°)/2LM measured under different HRRS configurations excited by a 2.41 eV laser.

ESI.† The theoretical results (circles in Fig. S2 of the ESI†) are in good agreement with the experimental values (crosses in Fig. S2 of the ESI†). More exactly, the LB force constant between graphene and MoS_2 is $\alpha^\perp(Gr/M) = 5.68 \times 10^{19}$ N m^{-3}. The LB force constant between graphene and hBN is $\alpha^\perp(Gr/hBN) = 7.83 \times 10^{19}$ N m^{-3}. $\alpha^\perp(Gr/M)$ is insensitive to the twisted angle between graphene and MoS_2 because moiré superlattices at the Gr/MoS_2 interface do not exist due to a large lattice mismatch between the two constituents.[17,18] $\alpha^\perp(Gr/M)$ and $\alpha^\perp(Gr/hBN)$ are comparable with those of MoS_2 ($\alpha^\perp(M)$=8.65 × 10^{19} N m^{-3}) and graphene ($\alpha^\perp(Gr) = 10.7 \times 10^{19}$ N m^{-3}) flakes. This makes lattice vibrations associated with the LBMs to well extend over the entire layers of the vdWHs. Thus, in contrast to the S modes, the peak positions of the LBMs in vdWHs are distinct from those of standalone 2LM and t($m+n$)LG.

According to crystal and phonon symmetry analysis of 2DMs and vdWHs,[28] the LBMs are helicity-conserved, while the S modes experience helicity changes. The helicity resolved Raman scattering (HRRS) experiments can thus enable the differentiation of the S modes and LBMs, especially when the S mode and LBM are overlapped. For example, the weak LBM$_{6,5}$ in t(3+1)LG(13°)/2LM can be revealed in the HRRS experiment under the (σ+,σ+) configuration, as demonstrated in Fig. 1(c). In contrast, LBM$_{6,5}$ is so weak that it cannot be distinguished from the strong C$_{3,2}$ and S$_{2,1}$ modes in the Raman spectra measured under the depolarized configuration (Fig. 1(b)). Therefore, in order to properly investigate IBPM for the LBMs in vdWHs, the adoption of the (σ+,σ+) configuration is significant for the selective detection of LBMs.

3.2. Peculiar resonance mechanism of LBMs in tMLG-based vdWHs

Figs. 2(a) and (b) show the Raman spectra of 2LM and t(3+1)LG (13°) under the (σ+,σ+) configuration excited by several E_{ex}, and the corresponding resonance profiles of the LBMs are depicted in Figs. 2(c) and (d), respectively. The LBMs in 2LM and t(3+1)LG (13°) are in resonance with the energy of the C exciton (E_C, ~2.65 eV) in MoS_2[30] and the VHS energy of JDOS (E_{VHS}) in t(3+1)LG (13°) (~2.3 eV), respectively. It should be noted that the LBM in 4LG is absent in its Raman spectrum due to the weak EPC.[13] In the following, the resonant Raman scattering of t($m+n$)LG/kLM and NLG/kLM ($N = m+n$) is studied for comparison to reveal how the resonance properties between LBMs and electronic states impact the Raman spectrum of vdWHs.

Figs. 2(e) and (f) show the Raman spectra of 4LG/2LM and t(3+1)LG(13°)/2LM under the (σ+,σ+) configuration excited by several E_{ex}, and the corresponding resonance profiles of the LBMs are depicted in Figs. 2(g) and (h), respectively. Because the strength of the interfacial coupling in t(3+1)LG is identical to that of the interlayer coupling in 4LG,[16] the frequency of the corresponding LBM in t(3+1)LG(13°)/2LM and 4LG/2LM should be equal to each other. Indeed, LBM$_{6,4}$ and LBM$_{6,5}$ are observed in the two vdWHs. LBM$_{6,4}$ exhibits an almost identical frequency and resonance profile for the two vdWHs. According to the interlayer displacements, LBM$_{6,4}$ is mainly
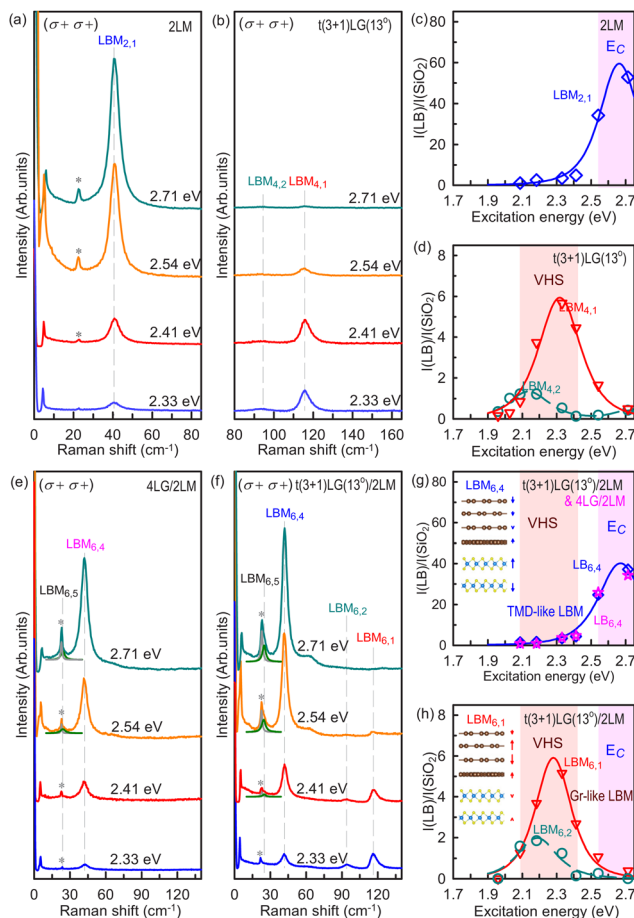

Fig. 2 Resonance behaviour of LBMs. (a and b) Raman spectra of 2LM (a) and t(3+1)LG(13°) (b) obtained under the (σ+,σ+) configuration. (c and d) The resonance profiles of LBM$_{2,1}$ in 2LM (c), LBM$_{4,1}$ and LBM$_{4,2}$ in t(3+1)LG(13°) (d). (e and f) Raman spectra of 4LG/2LM (e) and t(3+1)LG (13°)/2LM (f) obtained under the (σ+,σ+) configuration. (g and h) The resonance profiles and interlayer displacements of TMD-like LBM such as LBM$_{6,4}$ (g), Gr-like LBMs including LBM$_{6,1}$ and LBM$_{6,2}$ (h). The Raman experiments under discrete excitation energies in (c and d) and (g and h) are normalized by the E_1 mode of quartz (at ~127 cm^{-1}) to eliminate the efficiency difference of CCD under different excitation energies.[5,16,29] "*" in (a and e) indicates the residual S mode signal.

localized within the 2LM constituent and it is denoted as TMD-like LBM in t(3+1)LG(13°)/2LM and 4LG/2LM vdWHs. Similar to the cross-dimensional EPC effect in hBN/WS$_2$ vdWHs,[5] the resonance profiles of LBM$_{6,4}$ in t(3+1)LG(13°)/2LM and 4LG/2LM vdWHs are similar to those of LBM$_{2,1}$ in standalone 2LM flakes.

In contrast to the TMD-like LBMs, LBM$_{6,1}$ and LBM$_{6,2}$ can only be observed in t(3+1)LG(13°)/2LM, but not in 4LG/2LM. Because the interlayer displacements of the LBM$_{6,1}$ and LBM$_{6,2}$ are mainly localized in the t(3+1)LG(13°) constituent, the two LBMs are denoted as Gr-like LBMs. As more atomic layers are involved in the lattice vibration, the frequency of LBM$_{6,1}$ in t(3+1)LG(13°)/2LM is slightly higher than that of LBM$_{4,1}$ in standalone t(3+1)LG(13°). However, the resonance profiles of the two modes are similar to each other due to the cross-

dimensional EPC effect in t(3+1)LG(13°)/2LM. More LBMs present in t(3+1)LG(13°)/2LM indicate that one can selectively activate the LBMs in a vdWH by engineering its constituents *via* the coupling between the phonons of the vdWH and electrons of its constituent. In addition, one can manipulate the Raman intensity profile of the LBMs by the tuning electronic structure of the t($m+n$)LG constituent with changing θ_t, as E_{VHS} in t($m+n$)LG is sensitive to θ_t.[21]

Because the electronic structure of t($m+n$)LG is very sensitive to its θ_t,[15,16] it is expected that the intensity of the LBMs in t($m+n$)LG/kLM vdWHs can be tuned by selecting an appropriate E_{ex} to match E_{VHS} of the t($m+n$)LG constituent *via* the cross-dimensional EPC effect.[5] Here, we focus on two samples of t(2+1)LG(13°)/2LM and t(2+1)LG(17°)/2LM. The previous work also shows that E_{VHS} of t($m+1$)LG ($m > 1$) exhibits a broader range around that of t(1+1)LG.[15] According to the previous report on E_{VHS} of t(1+1)LG,[21] E_{ex} of 2.33 eV and 2.71 eV can match E_{VHS} of t(2+1)LG(13°) and t(2+1)LG(17°) constituents, respectively. Based on the above analysis, 2.33 eV and 2.71 eV were chosen to excite the Raman spectra of t(2+1) LG(13°)/2LM and t(2+1)LG(17°)/2LM, as shown in Figs. 3(a) and (c) for the LBMs under the helicity-resolved ($\sigma+$, $\sigma+$) configuration.
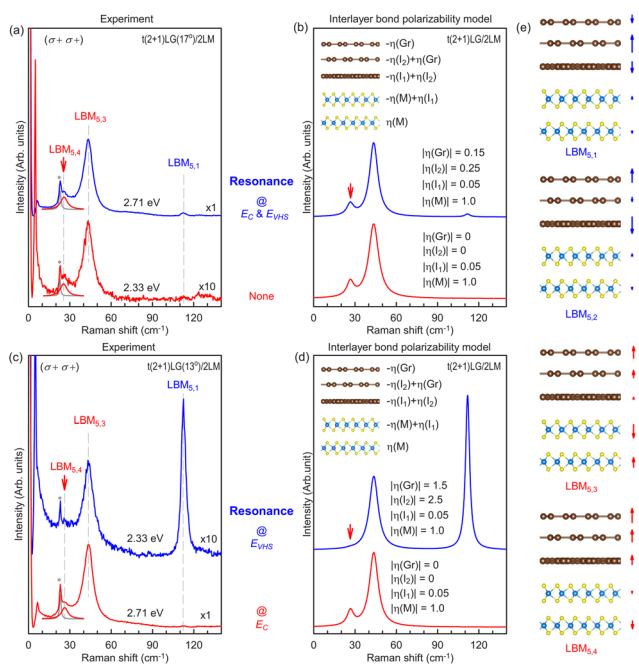
Fig. 3 Manipulating Raman intensity profile of LBMs by tuning the relative energy difference between E_{VHS} of t(2+1)LG and E_C of 2LM. (a and b) Experimental results under the ($\sigma+,\sigma+$) polarization configuration and theoretical simulation by vdWH-based IBPM of t(2+1)LG(17°)/2LM. (c and d) Experimental results and theoretical simulation by vdWH-based IBPM of t(2+1)LG(13°)/2LM. The insets and fitting parameters in both (b) and (d) show the schematic diagram of vdWH-based IBPM established for the corresponding vdWH. "*" indicates the residual S modes under the ($\sigma+,\sigma+$) polarization configuration. (e) Interlayer displacements of LBMs in t(2+1)LG/2LM.

When E_{ex} is not resonant with E_{VHS} of the t(2+1)LG constituent of the two vdWHs, LBM$_{5,1}$ cannot be clearly observed in the Raman experiment, while LBM$_{5,4}$ and LBM$_{5,3}$ of the two vdWHs exhibit similar intensity profiles (red curves in Figs. 3(a) and (c)). In contrast, when E_{ex} is resonant with E_{VHS} of the t(2+1)LG constituent, *i.e.*, t(2+1)LG(17°)/2LM and t(2+1)LG (13°)/2LM are excited by 2.71 eV and 2.33 eV, respectively, the two vdWHs exhibit some peculiar spectral features: (i) LBM$_{5,1}$ can be clearly observed in both vdWHs. The intensity of LBM$_{5,1}$ even exceeds that of LBM$_{5,3}$ when t(2+1)LG(13°)/2LM is excited by 2.33 eV. (ii) LBM$_{5,4}$ is too weak to be recognizable in t(2+1)LG(13°)/2LM. These results indicate that it is an effective way to selectively manipulate the intensity profile of LBMs in tMLG-based vdWHs by θ_t of tMLG.

3.3. Improved IBPM for tMLG-based ternary vdWHs

To quantitatively comprehend the above E_{ex}-dependent spectral features in t(2+1)LG/2LM vdWHs, we then improved IBPM of LBMs in standalone 2DM flakes[5,10,12] for the case of polynary vdWHs. According to the classical theory of Placzek approximation, the Raman intensity of a phonon mode q under the non-resonant condition is:[7,31]

$$I(q) \propto \frac{n_q+1}{\omega_q}\left|e_s \cdot \mathbf{R}(q) \cdot e_i^{\mathbf{T}}\right|^2$$
$$= \frac{n_q+1}{\omega_q}\left|\sum_{\mu\nu} e_{i,\mu} e_{s,\nu} \Delta\alpha_{\mu\nu}(q)\right|^2 \quad (1)$$

where n_q and ω_q are the phonon occupation according to Bose−Einstein statistics and peak position of the corresponding phonon mode, respectively, $\mathbf{R}(q)$ is the E_{ex}-independent Raman tensor of the phonon mode q, subscripts μ and ν indicate Cartesian components (x, y or z) of the tensor, and e_i and e_s are the unit vectors for the polarization of the incident and scattered light, respectively. $\Delta\alpha_{\mu\nu}$ (q) is the so-called Raman tensor element, which is strongly associated with the change of the system polarizability caused by the corresponding lattice vibration.[10] It can be obtained by differentiating each component of the polarizability tensor with respect to the atomic displacements from the equilibrium position:[10]

$$\Delta\alpha_{\mu\nu}(q) = \sum_{j\gamma}\left[\frac{\partial\alpha_{\mu\nu}}{\partial r_{j\gamma}}\right]_0 \Delta r_{j\gamma}(q)$$
$$= \sum_{j\gamma}\alpha'_{j\gamma,\mu\nu} \cdot \Delta r_{j\gamma}(q) \quad (2)$$

where $r_{j\gamma}$ is the position of atom j along the direction γ (x, y or z) in equilibrium, $\left[\frac{\partial\alpha_{\mu\nu}}{\partial r_{j\gamma}}\right]_0 = \alpha'_{j\gamma,\mu\nu}$ is the derivative of the electronic polarizability tensor element $\alpha_{\mu\nu}$ with respect to the atomic displacements from the equilibrium configuration, $\Delta r_{j\gamma}$ is the atomic displacement of atom j along γ direction. In general, when one analyzes the atomic displacements of a vibration mode, bond strengths and directions of all the atoms within a large size of a unit cell with many atoms are involved. Thus, the quantitative determination of total polarizability

change is computationally intensive,[7] leading to a challenge in quantitative prediction of the corresponding Raman intensity.

Fortunately, it is easy to estimate the polarizability change of layered materials induced by the atomic displacements of interlayer phonon vibrations from the equilibrium position.[10,12] Detailed analysis[12] shows that the Raman tensor elements $\Delta\alpha_{\mu\nu}(q)$ are directly connected with the equilibrium configuration bond vector normalized to unity, the bond length in equilibrium, and the radial derivatives of the bond polarizabilities with respect to the bond length. For an interlayer mode in standalone 2DM flakes, only the bonds between the layers (interlayer bonds) are altered during such a vibration, leading to the polarizability change. In this case, the total change of the system polarizability by the interlayer vibration is a sum of the changes of each layer (denoted as i), which is the product of the derivative $(\vec{\alpha}'_{i,\mu\nu})$ of the system polarizability with respect to the interlayer displacements of the i layer and its displacement $(\Delta\vec{r}_i)$ from the equilibrium position, $i.e.$, $\Delta\alpha_{\mu\nu} = \sum_i \vec{\alpha}'_{i,\mu\nu} \cdot \Delta\vec{r}_i = \sum_i (\alpha'_{ix,\mu\nu}\Delta r_{ix} + \alpha'_{iy,\mu\nu}\Delta r_{iy} + \alpha'_{iz,\mu\nu}\Delta r_{iz})$, where $\alpha'_{ix,\mu\nu}$ (or $\alpha'_{iz,\mu\nu}$) is the polarizability derivative with respect to the ith layer's displacement along the x (or z) direction, and (Δr_{ix}) (or Δr_{iz}) is the ith layer's displacement along the x (or z) direction in the interlayer vibration (x for the shear modes and z for the LBMs). Further analysis[12] directly shows that $\vec{\alpha}'_{i,\mu\nu}$ can be determined by the interlayer bonds (length and direction), and interlayer bond polarizability.

For standalone 2DM flakes and the corresponding vdWHs, the LBMs can only be observed in parallel linear- and circular-polarization configurations, and their Raman tensor has a concise form:[14]

$$A = \begin{bmatrix} \Delta\alpha_{xx} & 0 & 0 \\ 0 & \Delta\alpha_{yy} & 0 \\ 0 & 0 & \Delta\alpha_{zz} \end{bmatrix} \quad (3)$$

where $\Delta\alpha_{xx} = \Delta\alpha_{yy}$. Under helicity-resolved ($\sigma+,\sigma+$) configuration, based on eqn (1), the Raman intensity of LBMs can be calculated as follows:

$$I(\text{LBM}) \propto \frac{n_{\text{LBM}} + 1}{\omega_{\text{LBM}}} |\Delta\alpha_{xx}|^2$$
$$= \frac{n_{\text{LBM}} + 1}{\omega_{\text{LBM}}} \left| \sum_i \alpha'_{iz,xx} \cdot \Delta r_{iz} \right|^2 \quad (4)$$

It is clear that only $\alpha'_{iz,xx}$ and Δr_{iz} contribute to the Raman intensity of the LBM under the ($\sigma+,\sigma+$) configuration. For convenience, we denote $\alpha'_{iz,xx}$ and Δr_{iz} as α'_i and Δz_i, respectively, and therefore, $I(\text{LBM}) \propto \left| \sum_i \alpha'_i \cdot \Delta z_i \right|^2$. Such an empirical approach to estimate Raman intensity of the LBMs is referred to as the IBPM.[10,12]

Under non-resonant conditions, the imaginary part of the electric polarizability tensor elements can be ignored, so α'_i can be given by real numbers. For a standalone N-layer ($N > 2$)

2DM flake, the interlayer bond length, the interlayer bond polarizability and its radial derivative for each interlayer bond can be treated as constants,[10,12] thus, the contribution of all the interlayer bonds between the layer i and its adjacent layer $i - 1$ (or $i + 1$) to the derivative of the electronic polarizability of layer i with respect to its atomic displacement from the equilibrium configuration can also be treated as a constant, denoted as $\eta_{i,i-1}$ (or $\eta_{i,i+1}$). For an interior layer i ($1 < i < N$), $\alpha'_i = \eta_{i,i-1} + \eta_{i,i+1}$. Because the interlayer bond strengths between the interior layer i and its two equivalent adjacent layers are the same but the bond vectors of their z component are opposite, the cancellation effect from the two neighboring layers can result in $\eta_{i,i-1} = -\eta_{i,i+1}$ ($1 < i < N$), leading to $\alpha'_i = 0$ ($1 < i < N$). In contrast, the surface layer ($i = 1$ or N) has only one adjacent layer, α'_1 ($= \eta_{1,2}$) and α'_N ($= \eta_{N,N-1}$) usually hold non-zero values and $\alpha'_1 = -\alpha'_N$; thus $\eta_{1,2}$ of the standalone N-layer ($N > 1$) 2DM flake is an intrinsic parameter of the 2DM. One can denote $\eta_{1,2}$ as $\eta(2\text{DM})$, $e.g.$, $\eta(\text{Gr})$, $\eta(\text{M})$, $\eta(\text{BN})$ for $\eta_{1,2}$ of graphene, MoS_2 and hBN multilayer flakes, respectively.

Next, we improve IBPM to the case for binary and polynary vdWHs, in which an interface exists between A and B multilayer constituents of the vdWH and the adjacent layers of the interface is the non-equivalent i^{th} and $(i + 1)^{th}$ layers. Accordingly, $\eta_{i,i+1}$ describes the contribution of all the interlayer bonds between the layer i in constituent A and its adjacent $(i + 1)$ layer in constituent B to the derivative of the electronic polarizability of layer i with respect to its atomic displacement from the equilibrium configuration. It is an intrinsic parameter for the interface between A and B constituents, which can be denoted as $\eta(I)$. It should be noted that $\eta_{i+1,i} = -\eta_{i,i+1} = -\eta(I)$. $\eta(I)$ is usually different from $\eta(A)$ and $\eta(B)$, leading to non-zero α'_i ($= -\eta(A) + \eta(I)$) and α'_{i+1} ($= -\eta(I) + \eta(B)$) for the layers adjacent to the interface. In particular, t($m+n$)LG is a special vdWH, α'_m should be non-zero because of the two non-equivalent graphene layers adjacent to the interface, $i.e.$, $\eta_{m,m+1} = \eta(I)$, $\eta_{m+1,m} = -\eta(I)$. Here, $\eta(I)$ is usually not equal to $\eta(\text{Gr})$. Based on this point, t(2+1)LG/2LM is actually a ternary vdWH.

Under the resonant Raman conditions, α'_i is also dependent on the band structure of the corresponding constituent, exhibiting E_{ex} dependence. In this case, one cannot neglect the imaginary term of the electric polarizability tensor elements. Thus, η for the constituents and interface should be a complex value. According to above improved approach, in the t(2+1)LG/2LM vdWH, the α'_i of each layer can be simply described by $\alpha'_1 = \eta(\text{M})$, $\alpha'_2 = -\eta(\text{M}) + a(I_1)$, $\alpha'_3 = -\eta(I_1) + \eta(I_2)$, $\alpha'_4 = -\eta(I_2) + \eta(\text{Gr})$, $\alpha'_5 = -\eta(\text{Gr})$, where $\eta(I_1)$ and $\eta(I_2)$ are parameters for the interface of MoS_2/graphene and graphene/graphene, respectively. Finally, the total change of polarizability of the system for the LBM is given by:

$$\Delta\alpha = \Delta\alpha_{xx} = \sum_i \alpha'_i \cdot \Delta z_i$$
$$= \eta(M)[\Delta z_1 - \Delta z_2] + \eta(I_1)[\Delta z_2 - \Delta z_3]$$
$$+ \eta(I_2)[\Delta z_3 - \Delta z_4] + \eta(Gr)[\Delta z_4 - \Delta z_5] \quad (5)$$

The complex value η can be denoted as $\eta = |\eta|e^{i\varphi}$. Based on the above IBPM, we set $|\eta(M)| = 1$ as a fixed parameter and fit

Table 1 Fitting parameters and resonance conditions (Res. Cond.) of vdWH-based IBPMs established for t(2+1)LG(17°)/2LM and t(2+1)LG (13°)/2LM

Res. Cond.	t(2+1)LG(17°)/2LM		t(2+1)LG(13°)/2LM	
	@2.33 eV –	@2.71 eV E_C &E_{VHS}	@2.71 eV E_C	@2.33 eV E_{VHS}
$|\eta(Gr)|$	0.0	0.15	0.0	1.5
$|\eta(I_2)|$	0.0	0.25	0.0	2.5
$|\eta(I_1)|$	0.05	0.05	0.05	0.05
$|\eta(M)|$	1	1	1	1

the corresponding Raman intensity profile of all the LBMs in the vdWH. The fitted moduli for each η are listed in the Table 1. The fitted $\varphi(I_2)$ is π, and $\varphi(I_1)$, $\varphi(Gr)$ and $\varphi(M)$ are 0. $|\eta(Gr)|$ and $|\eta(I_2)|$ are dependent on E_{ex}, illustrating how the resonance behavior of the LBM affects its modulus and the phase of the corresponding Raman tensor.

3.4. Understanding the LBM intensity profile for tMLG-based ternary vdWHs

Now, we explain the Raman spectra of the two t(2+1)LG/2LM vdWHs in Figs. 3(a) and (c) based on the improved IBPM in detail. When the E_{ex} is not resonant with the E_{VHS} of t(2+1)LG constituent, *i.e.*, 2.33 eV-excited t(2+1)LG(17°)/2LM and 2.71 eV-excited t(2+1)LG(13°)/2LM (red curves in Figs. 3(a) and (c)), the fitted $|\eta(I_2)|$ and $|\eta(Gr)|$ are zero, thus the total change of polarizability for all the LBMs is mainly contributed by the MoS$_2$ constituent and the corresponding interface. According to the eqn (5), the total change of polarizability for LBM$_{5,1}$ is negligible due to its localized atomic displacement within the t(2+1)LG constituent ($\Delta z_1 - \Delta z_2 \sim 0$), leading to undetectable intensity in Raman spectra. As for LBM$_{5,3}$ and LBM$_{5,4}$, the normalized $|\eta(I_1)|$ to $|\eta(M)|$ is the same for the two vdWHs. According to the eqn (5), LBM$_{5,4}$ and LBM$_{5,3}$ exhibit similar intensity profiles, as indicated by the fitting in Figs. 3(b) and (d).

When E_{ex} is resonant with E_{VHS} of the t(2+1)LG constituent, *i.e.*, 2.71 eV-excited t(2+1)LG(17°)/2LM and 2.33 eV-excited t(2+1)LG(13°)/2LM, $|\eta(Gr)|$ and $|\eta(I_2)|$ reach their maximum values. Under this condition, the polarizability change caused by the lattice vibrations related with graphene layers is crucial. For LBM$_{5,1}$, its atomic displacement is mainly confined in the t(2+1)LG constituent, leading to positive $\Delta z_4 - \Delta z_5$ and negative $\Delta z_3 - \Delta z_4$. In principle, this cancellation effect would result in weak intensity for LBM$_{5,1}$. However, resonant excitation of the t(2+1)LG constituent leads to different phases between $\varphi(Gr)$ and $\varphi(I_2)$, *i.e.*, $\varphi(Gr) = 0$, $\varphi(I_2) = \pi$. Therefore, LBM$_{5,1}$ becomes observable for resonantly excited t(2+1)LG constituent in the two vdWHs. Particularly, LBM$_{5,1}$ reaches maximum intensity relative to LBM$_{5,3}$ for 2.33 eV-excited t(2+1)LG(13°)/2LM because its $|\eta(Gr)|$ and $|\eta(I_2)|$ are even larger than $|\eta(M)|$.

Next, we turn to LBM$_{5,4}$. Its intensity depends on the sum of $\eta(M)[\Delta z_1 - \Delta z_2] + \eta(I_1)[\Delta z_2 - \Delta z_3]$ and $\eta(I_2)[\Delta z_3 - \Delta z_4] + \eta(Gr)[\Delta z_4 - \Delta z_5]$. The latter term possesses an opposite sign to the former term for the resonant case of the t(2+1)LG constitu-

ent based on the fitted $\eta(M)$, $\eta(Gr)$, $\eta(I_1)$ and $\eta(I_2)$. This cancellation effect is slightly different for the two vdWHs: in 2.71 eV-excited t(2+1)LG(17°)/2LM, $|\eta(M)|$ is much larger than $|\eta(I_2)|$ and $|\eta(Gr)|$, the cancellation effect is not so strong that LBM$_{5,4}$ can be recognized in the Raman spectrum. However, in 2.33 eV-excited t(2+1)LG(13°)/2LM, the larger $|\eta(I_2)|$ and $|\eta(Gr)|$ than $|\eta(M)|$ makes the total change of polarizability to be very small, leading to very weak LBM$_{5,4}$ consistent with the undetectable LBM$_{5,4}$ in the experiment.

The different spectral features of LBM$_{5,1}$ and LBM$_{5,4}$ in the two vdWHs reveal that the derivative of the electronic polarizability of the constituent can be manipulated by its resonance conditions. Moreover, the resonance condition of one constituent can modulate the derivative of the electronic polarizability of its atomic layer near the interface and further modify the corresponding derivative of the electronic polarizability of adjacent atomic layer in other constituents. This opens the possibility that interlayer phonon spectra can be manipulated by selecting the excitation energy to match the transition energies of specific constituents. One can notice that $|\eta(Gr)|$ and $|\eta(I_2)|$ of t(2+1)LG(17°)/2LM are different from those of t(2+1)LG(13°)/2LM under the same E_{ex}, respectively. This means that the fitted $|\eta|$ for the specific constituent and interface is an indication of resonance conditions for the corresponding constituent in the vdWHs.

3.5. Generalizing the improved IBPM to polynary vdWHs

As mentioned above, standalone mL-hBN exhibits no observable LBM due to its extremely weak EPC strength.[18] However, when t(m+n)LG is stacked beneath the hBN flakes, *e.g.*, 24L-hBN/t(1+1)LG(17°), the LBMs of vdWH are significantly enhanced, displaying uniformly distributed Raman intensities across a wide spectral range when the E_{ex} matches E_{VHS} of the t(1+1)LG constituent, as depicted in Fig. 4(a). Furthermore, by introducing a monolayer MoS$_2$ as the bottom layer to form 24L-hBN/t(1+1)LG(17°)/1LM, the corresponding Raman spectrum exhibits a striking difference compared to the original one of 24L-hBN/t(1+1)LG(17°), *i.e.*, the disappearance of LBMs in the frequency range of 50–80 cm^{-1}, as illustrated in Fig. 4(a). Fig. 4(b) presents a comparison of the IBPM for the two vdWHs. By setting $|\eta(I_2)|$ = 1.0, the experimental curve of 24L-hBN/t(1+1)LG(17°) can be simulated well by the fitting parameters of $|\eta(BN)|$ = 0 and $|\eta(I_3)|$ = 0.05, as shown in Fig. 4(c). However, to properly reproduce the experimental curve of 24L-hBN/t(1+1)LG(17°)/1LM by the IBPM, an additional parameter $|\eta(I_1)|$ = 0.05 is necessary for the interface between graphene and MoS$_2$, and the determined phases for $\eta(I_1)$, $\eta(I_2)$ and $\eta(I_3)$ are zero. Careful check reveals that the disappearance of the LBMs in the frequency range of 50–80 cm^{-1} results from the cancellation effect of $\Delta\alpha$ induced by the interfacial coupling between t(1+1)LG and MoS$_2$. This mechanism is similar to the disappearance of LBM$_{5,4}$ in t(2+1)LG(13°)/2LM excited by 2.33 eV.

A similar effect occurs for 44L-hBN/t(2+1)LG(15°) and 44L-hBN/t(2+1)LG(15°)/2LM. The introduction of 2LM below 44L-hBN/t(2+1)LG(15°) as the bottom layer results in a different
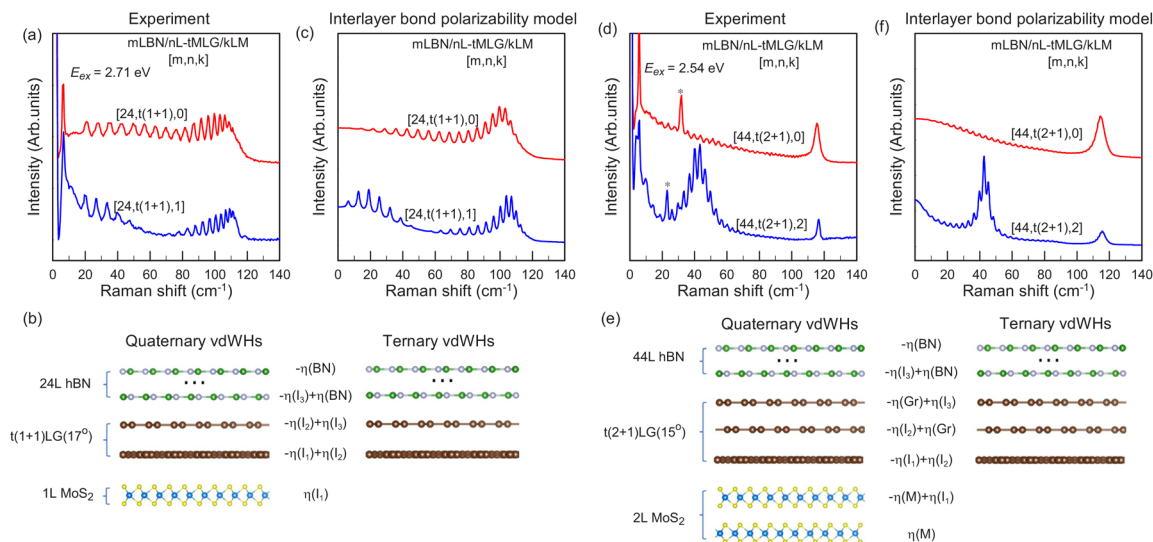
Fig. 4 vdWH-based IBPM to mL-hBN/t($m+n$)LG and mL-hBN/t($m+n$)LG/kLM. (a) Raman spectra and (b) the corresponding schematics of vdWH-based IBPMs for 24L-hBN/t(1+1)LG(17°) and 24L-hBN/t(1+1)LG(17°)/1LM vdWHs. (c) Intensity profile of LBMs simulated by vdWH-based IBPMs. (d) Raman spectra and (e) the corresponding schematics of vdWH-based IBPMs for 44L-hBN/t(2+1)LG(15°) and 44L-hBN/t(2+1)LG(15°)/2LM vdWHs. "*" indicates the residual S(C) modes. (f) Calculated relative intensities of LBMs. The experimental results in (a) and (d) are demonstrated under the ($\sigma+,\sigma+$) configuration.

intensity profile of the LBMs, as depicted in Fig. 4(d). Fig. 4(e) shows the IBPM diagram for the two vdWHs. To produce the intensity profile of the LBMs for the corresponding vdWHs by the IBPM, the fitted phase is $\varphi_{I2} = \pi$, and the fitted ratio is $|\eta(I_2)|/|\eta(\text{Gr})| = 5/3$, which are in good agreement with the case for t(2+1)LG/2LM in Figs. 3(a) and (c). All the fitted parameters are depicted in Table 2 for 44L-hBN/t(2+1)LG(15°) and the corresponding simulated spectra are shown in Fig. 4(f), which exhibit consistency with the experimental findings.

Finally, we check the case of quaternary vdWH, 44L-hBN/t(2+1)LG(15°)/2LM excited by $E_{\text{ex}} = 2.54$ eV (resonant with E_C of 2LM), and similarly, we set $|\eta(\text{M})| = 1$. The incorporation of 2LM to 44L-hBN/t(2+1)LG(15°) results in a different intensity profile of the LBMs, as depicted in Fig. 4(d). It can be reproduced well by the improved IBPM (Fig. 4(e)), as shown in Fig. 4(f), and the corresponding fitting parameters are summarized in Table 2. It is found that the fitted ratio between $|\eta(I_2)|$ and $|\eta(\text{Gr})|$ is also equal to 5/3, consistent with the pre-

vious result in Fig. 3. This further indicates that the improved IBPM can be applied to tMLG-based polynary vdWHs up to three interfaces.

It should be noted that the E_{VHS} of t(1+1)LG(17°) and t(2+1)LG(15°) are comparable to E_C of 2LM. When the excitation energy is chosen to match E_{VHS} of t(1+1)LG(17°) and t(2+1)LG(15°), resonance Raman scattering can occur for both MoS$_2$ and tMLG constituents, resulting in rich LBMs over a wide spectral range 0–120 cm^{-1}.

The above discussions indicate that, for a given polynary vdWH, the improved IBPM model and the corresponding fitting parameters are determined. However, the resonance conditions of each constituent can significantly modify the values of the fitting parameters in the improved IBPM model, leading to dramatically different intensity distributions for the observed LBMs. Therefore, one can delineate the resonance information of each constituent according to the fitted $|\eta|$ parameters for the observed LBMs in polynary vdWHs.

4. Conclusions

This study presents a comprehensive investigation of the Raman intensity profile and resonance behaviors of LBMs in tMLG-based polynary vdWHs, through leveraging the resonance Raman technique and helicity-resolved Raman scattering. The LB phonons exhibit strong coupling with the electronic states confined in specific constituents and we proposed an improved IBPM by considering the contribution from multiple interfaces and the resonance from VHSs of JDOS in standalone 2DM and tMLG flakes, to comprehensively understand

Table 2 Fitting parameters of vdWH-based IBPMs established for polynary vdWHs mL-hBN/nL-tMLG/kLM [m,n,k]

	mL-hBN/nL-tMLG/kLM [m,n,k]			
	[24,t(1+1),0]	[24,t(1+1),1]	[44,t(2+1),0]	[44,t(2+1),2]
$|\eta(\text{BN})|$	0	0	0	0
$|\eta(I_3)|$	0.05	0.05	0.05	0.05
$|\eta(\text{Gr})|$	—	—	0.6	0.3
$|\eta(I_2)|$	1	1	1	0.5
$|\eta(I_1)|$	—	0.05	—	0.05
$|\eta(\text{M})|$	—	—	—	1

the intensity profiles of LBMs in resonance/non-resonance Raman scattering. The simulated results reproduce well the intensity profiles of LBMs in tMLG-based ternary and quaternary vdWHs, which are sensitive to the excitation energy and the θ_t of the tMLG constituent. Our investigation suggests that the improved IBPM has great potential in understanding and predicting the relative intensity of LBMs in polynary vdWHs, also offering a novel avenue to manipulate the Raman intensity profile of LBMs.

Author contributions

P.-H. Tan conceived the idea and directed and supervised the project. R. Mei and P.-H. Tan designed the experiments. R. Mei performed the experiments, assisted by L.-S. Chen, Y.-M. Shi and Z.-M. Wei. R. Mei and H. Wu prepared the samples. R. Mei, M.-L. Lin and P.-H. Tan analyzed the data; R. Mei and P.-H. Tan wrote the manuscript with input from all authors.

Conflicts of interest

There are no conflicts to declare.

Acknowledgements

References

1 A. C. Ferrari and D. M. Basko, *Nat. Nanotechnol.*, 2013, **8**, 235–246.

2 X. Zhang, X.-F. Qiao, W. Shi, J.-B. Wu, D.-S. Jiang and P.-H. Tan, *Chem. Soc. Rev.*, 2015, **44**, 2757–2785.

3 M. Cardona, *Light Scattering in Solids I: Introductory Concepts | SpringerLink*, Springer, Berlin, 1983, vol. 8.

4 B. R. Carvalho, L. M. Malard, J. M. Alves, C. Fantini and M. A. Pimenta, *Phys. Rev. Lett.*, 2015, **114**, 136403.

5 M.-L. Lin, Y. Zhou, J.-B. Wu, X. Cong, X.-L. Liu, J. Zhang, H. Li, W. Yao and P.-H. Tan, *Nat. Commun.*, 2019, **10**, 2419.

6 R. Loudon, *Adv. Phys.*, 1964, **13**, 423–482.

7 S. Guha, J. Menéndez, J. B. Page and G. B. Adams, *Phys. Rev. B: Condens. Matter Mater. Phys.*, 1996, **53**, 13106–13114.

8 R. Saito, M. Furukawa, G. Dresselhaus and M. S. Dresselhaus, *J. Phys.: Condens. Matter*, 2010, **22**, 334203.

9 J. Van Baren, G. Ye, J.-A. Yan, Z. Ye, P. Rezaie, P. Yu, Z. Liu, R. He and C. H. Lui, *2D Mater.*, 2019, **6**, 025022.

10 X. Luo, X. Lu, C. Cong, T. Yu, Q. Xiong and S. Y. Quek, *Sci. Rep.*, 2015, **5**, 14565.

11 C. H. Lui, Z. Ye, C. Keiser, E. B. Barros and R. He, *Appl. Phys. Lett.*, 2015, **106**, 041904.

12 L. Liang, A. A. Puretzky, B. G. Sumpter and V. Meunier, *Nanoscale*, 2017, **9**, 15340–15355.

13 P. H. Tan, W. P. Han, W. J. Zhao, Z. H. Wu, K. Chang, H. Wang, Y. F. Wang, N. Bonini, N. Marzari, N. Pugno, G. Savini, A. Lombardo and A. C. Ferrari, *Nat. Mater.*, 2012, **11**, 294–300.

14 X. Zhang, W. P. Han, J. B. Wu, S. Milana, Y. Lu, Q. Q. Li, A. C. Ferrari and P. H. Tan, *Phys. Rev. B: Condens. Matter Mater. Phys.*, 2013, **87**, 115413.

15 J.-B. Wu, X. Zhang, M. Ijäs, W.-P. Han, X.-F. Qiao, X.-L. Li, D.-S. Jiang, A. C. Ferrari and P.-H. Tan, *Nat. Commun.*, 2014, **5**, 5309.

16 J.-B. Wu, Z.-X. Hu, X. Zhang, W.-P. Han, Y. Lu, W. Shi, X.-F. Qiao, M. Ijiäs, S. Milana, W. Ji, A. C. Ferrari and P.-H. Tan, *ACS Nano*, 2015, **9**, 7440–7449.

17 H. Li, J.-B. Wu, F. Ran, M.-L. Lin, X.-L. Liu, Y. Zhao, X. Lu, Q. Xiong, J. Zhang, W. Huang, H. Zhang and P.-H. Tan, *ACS Nano*, 2017, **11**, 11714–11723.

18 H. Wu, M.-L. Lin, Y.-C. Leng, X. Chen, Y. Zhou, J. Zhang and P.-H. Tan, *npj 2D Mater. Appl.*, 2022, **6**, 87.

19 F. Ren, B. Liu, Z. Chen, Y. Yin, J. Sun, S. Zhang, B. Jiang, B. Liu, Z. Liu, J. Wang, M. Liang, G. Yuan, J. Yan, T. Wei, X. Yi, J. Wang, Y. Zhang, J. Li, P. Gao, Z. Liu and Z. Liu, *Sci. Adv.*, 2021, **7**, eabf5011.

20 K. Kim, S. Coh, L. Z. Tan, W. Regan, J. M. Yuk, E. Chatterjee, M. F. Crommie, M. L. Cohen, S. G. Louie and A. Zettl, *Phys. Rev. Lett.*, 2012, **108**, 246103.

21 G. S. N. Eliel, M. V. O. Moutinho, A. C. Gadelha, A. Righi, L. C. Campos, H. B. Ribeiro, P.-W. Chiu, K. Watanabe, T. Taniguchi, P. Puech, M. Paillet, T. Michel, P. Venezuela and M. A. Pimenta, *Nat. Commun.*, 2018, **9**, 1221.

22 A. Vela, M. V. O. Moutinho, F. J. Culchac, P. Venezuela and R. B. Capaz, *Phys. Rev. B*, 2018, **98**, 155135.

23 H. Hao, M.-L. Lin, B. Xu, H. Wu, Y. Wang, H. Peng, P.-H. Tan, L. Tong and J. Zhang, *ACS Nano*, 2023, **17**, 10142–10151.

24 H. Patel, L. Huang, C.-J. Kim, J. Park and M. W. Graham, *Nat. Commun.*, 2019, **10**, 1445.

25 A. C. Ferrari, J. C. Meyer, V. Scardaci, C. Casiraghi, M. Lazzeri, F. Mauri, S. Piscanec, D. Jiang, K. S. Novoselov, S. Roth and A. K. Geim, *Phys. Rev. Lett.*, 2006, **97**, 187401.

26 F. Pizzocchero, L. Gammelgaard, B. S. Jessen, J. M. Caridad, L. Wang, J. Hone, P. Bøggild and T. J. Booth, *Nat. Commun.*, 2016, **7**, 11894.

27 K. L. Haley, J. A. Cloninger, K. Cerminara, R. M. Sterbentz, T. Taniguchi, K. Watanabe and J. O. Island, *Nanomanufacturing*, 2021, **1**, 49–56.

28 S.-Y. Chen, C. Zheng, M. S. Fuhrer and J. Yan, *Nano Lett.*, 2015, **15**, 2526–2532.

29 E. Vella, F. Messina, M. Cannas and R. Boscaino, *Phys. Rev. B: Condens. Matter Mater. Phys.*, 2011, **83**, 174201.

30 Y. Li, A. Chernikov, X. Zhang, A. Rigosi, H. M. Hill, A. M. van der Zande, D. A. Chenet, E.-M. Shih, J. Hone and T. F. Heinz, *Phys. Rev. B: Condens. Matter Mater. Phys.*, 2014, **90**, 205422.

31 M. Lazzeri and F. Mauri, *Phys. Rev. Lett.*, 2003, **90**, 036401.